Materials Science and Engineering A 391 (2005) 408–417

www.elsevier.com/locate/msea

Plasticity and damage in aluminum syntactic foams deformed under dynamic and quasi-static conditions

Dorian K. Balch[a,1], John G. O'Dwyer[b], Graham R. Davis[c], Carl M. Cady[d], George T. Gray III[d], David C. Dunand[a,*]

[a] *Northwestern University, Evanston, IL, USA*
[b] *Waterford Institute of Technology, Ireland*
[c] *Queen Mary, University of London, UK*
[d] *Los Alamos National Laboratory, Los Alamos, NM, USA*

Received 26 January 2004; received in revised form 2 September 2004; accepted 9 September 2004

Abstract

Syntactic foams were fabricated by liquid metal infiltration of commercially pure and 7075 aluminum into preforms of hollow ceramic microspheres. The foams exhibited peak strengths during quasi-static compression ranging from −100 to −230 MPa, while dynamic compression loading showed a 10–30% increase in peak strength magnitude, with strain rate sensitivities similar to those of aluminum–matrix composite materials. X-ray tomographic investigation of the post-compression loaded foam microstructures revealed sharp differences in deformation modes, with the unalloyed-Al foam failing initially by matrix deformation, while the alloy–matrix foams failed more abruptly through the formation of sharp crush bands oriented at about 45° to the compression axis. These foams displayed pronounced energy-absorbing capabilities, suggesting their potential use in packaging applications or for impact protection; proper tailoring of matrix and microsphere strengths would result in optimized syntactic foam properties.

Keywords: Syntactic foam; Aluminum alloys; Energy absorption; Dynamic compression; Strain rate sensitivity; X-ray tomography

1. Introduction

As compared to fully-dense metals and alloys, metallic foams exhibit low densities, high specific stiffnesses, high energy-absorbing capabilities, and good mechanical and acoustic damping capacities, among other attributes [1–3]. This combination of properties makes metallic foams an attractive choice for structural applications such as foam sandwich cores, fireproof and sound-damping panels, energy-absorbing packaging, and underwater buoyant structures. A particular class of foam structure, syntactic foams, consists of hollow spheres embedded in a continuous matrix. Such foams are primarily made with polymeric matrices and spheres [4–6], but metallic syntactic foams containing hollow ceramic spheres can also be fabricated using traditional metal matrix composite casting techniques [7,8]. Such aluminum/alumina sphere and aluminum/silica–alumina sphere foams have higher densities than conventional aluminum foams produced, e.g., by gas entrapment in the melt [2,9] or infiltration of salt preforms [10], but they have the advantages of higher strengths, isotropic mechanical properties, and excellent energy-absorbing capabilities due to extensive strain accumulation at relatively high stresses [8]. Also, their closed-cell geometry is attractive for mechanical and insulating properties.

As reviewed by, e.g., Refs. [1,2], the deformation of metallic foams has been the subject of numerous studies, which have mainly focused on conventional open- and closed-cell metallic foams. The few studies existing on metallic syntactic foams [7,8,11,12] have shown excellent energy-absorbing ca-

* Corresponding author. Tel.: +1 847 491 5370; fax: +1 847 467 6573.
E-mail address: dunand@northwestern.edu (D.C. Dunand).
[1] Present address: Sandia National Laboratories, Livermore, CA, USA.

0921-5093/$ – see front matter © 2004 Elsevier B.V. All rights reserved.
doi:10.1016/j.msea.2004.09.012

pabilities during quasi-static compression. To the best of our knowledge, there has been no examination of the dynamic compression of aluminum–matrix syntactic foams, of relevance for energy-absorbing applications, e.g., for packaging, armor, or automotive applications. The present study examines the high-strain rate compression of aluminum syntactic foams, as well as the quasi-static deformation and damage evolution of these foams using X-ray tomography, a non-destructive technique that allows for excellent resolution of internal features within metallic foams [13–16].

2. Experimental methods

2.1. Fabrication

Molten commercial-purity aluminum (cp-Al) and 7075-Al alloy were infiltrated into packed beds of ceramic microspheres using a custom-built vacuum/pressure infiltrator, described in Ref. [12]. The microspheres were composed of a mixture of 45 vol.% crystalline mullite ($3Al_2O_3$–$2SiO_2$) and 55 vol.% amorphous silica (SiO_2), and had diameters of 15–75 μm, wall thicknesses of 2–5 μm, and densities of 0.6–0.8 g/cm^3 (all information provided by the supplier, Envirospheres Pty Ltd.). The method of infiltration is described in detail elsewhere [17], and is summarized briefly. A 50 mm diameter graphite crucible was tap-packed with microspheres to a height of 80–120 mm. An ingot of aluminum was placed above the microspheres, separated by a 3 mm thick layer of alumina felt. The felt prevented contact between the melt and the spheres before pressure was applied, and also partially filtered the aluminum oxide layer during infiltration. After flushing with argon, the infiltrator was heated under mechanical vacuum until the aluminum melted and formed a seal across the width of the crucible. Argon gas was then rapidly introduced into the chamber, reaching a pressure of 3.5 MPa within 30 s, thereby forcing the molten aluminum at temperatures between 700 and 720 °C into the evacuated spaces between the hollow microspheres. Solidification occurred under 3.5 MPa pressure at a cooling rate of ca. 10 °C/min, with the resulting foam having minimal unintentional porosity in the center of the casting. Regions at the bottom of the castings were only partially infiltrated due to freezing of the infiltration front; this material was not used for experiments.

The foam produced with 7075-Al was heat-treated after sectioning to both an annealed (O) and a standard peak-aged (T6) temper [18]. Homogenization was performed in air at 470 °C for 24 h. Annealing was performed at 415 °C for 3 h, followed by controlled cooling to 230 °C at 45 °C/h, and a hold at 230 °C for 2.75 h. Peak-aging was achieved via heat treatment in air at 120 °C for 36 h. All heat treatments were completed with a water quench. In order to minimize room temperature aging, which can degrade the mechanical properties of 7075-Al [18], the samples were stored at −75 °C in a dry ice/ethanol bath during the ca. 3 h interval between homogenization and heat treatment. Samples for metallography, density measurement, and mechanical testing were machined from the as-infiltrated cp-Al and heat-treated 7075-O and -T6 materials using a low-speed diamond saw. Metallographic samples were polished using SiC paper, followed by 6 and 1 μm water-based diamond suspensions, and examined by optical microscopy. Density measurements were performed using a helium pycnometer.

2.2. Compression testing

Quasi-static compression testing was performed on parallelepiped samples with square cross-sectional areas of 25–38 mm^2 and length-to-width ratios of 2.2; engineering strains in excess of −60% were reached. Testing was carried out at constant crosshead speed with an initial strain rate of 10^{-3} s^{-1}. Strains were calculated from the crosshead displacement, corrected for deflection of the load frame. A compression cage with oil-lubricated tungsten carbide platens was used to ensure proper alignment and minimize sample barreling.

Dynamic compression tests were conducted on cylindrical samples 5.0 mm in diameter by 5.0 mm in length to engineering strains of ca. −13%. Testing was performed at strain rates of ca. 2300 s^{-1} utilizing a modified split-Hopkinson pressure bar (SHPB) [19] equipped with 9.4 mm diameter Ti–6Al–4V bars that improve the signal-to-noise level for low strength materials, as compared to the maraging steel bars traditionally utilized for SHPB studies on metals and alloys. The use of lower impedance titanium bars also facilitates the achievement of specimen stress equilibrium at lower strains, as the lack of stress equilibrium during initial load-up can make the determination of flow stresses inaccurate at high strain rates.

2.3. Post-compression X-ray tomography

X-ray microtomography was carried out on the quasi-statically deformed samples of cp-Al and 7075-T6 foam using the “MuCat” scanner at Queen Mary, University of London [20]. A high dynamic range digital charge coupled device (CCD) camera operated in time-delay integration mode was used in order to achieve high quality images free from ring artifacts. This scanner is designed to obtain very high definition images with a high signal-to-noise ratio, at the cost of data acquisition time. The specimens were scanned with an 8.7 μm voxel size with the X-ray acceleration potential and current set to 60 kV and 100 μA. For the cp-Al foam, five “blocks” of 1001 projections were recorded over a period of 48 h, while for the 7075-T6 foam, six blocks were recorded in 66 h, the specimens being translated along their rotation axes between blocks. The reconstructed blocks of data were assembled to form the final 3D image. The data set sizes for the cp-Al and 7075-T6 foams were $800 \times 800 \times 1030$ and $800 \times 800 \times 1164$ voxels (6.96 mm × 6.96 mm × 8.96 mm and 6.96 mm × 6.96 mm × 10.13 mm), respectively. Due to the length of time required for each scan, the 7075-O foam was not examined.

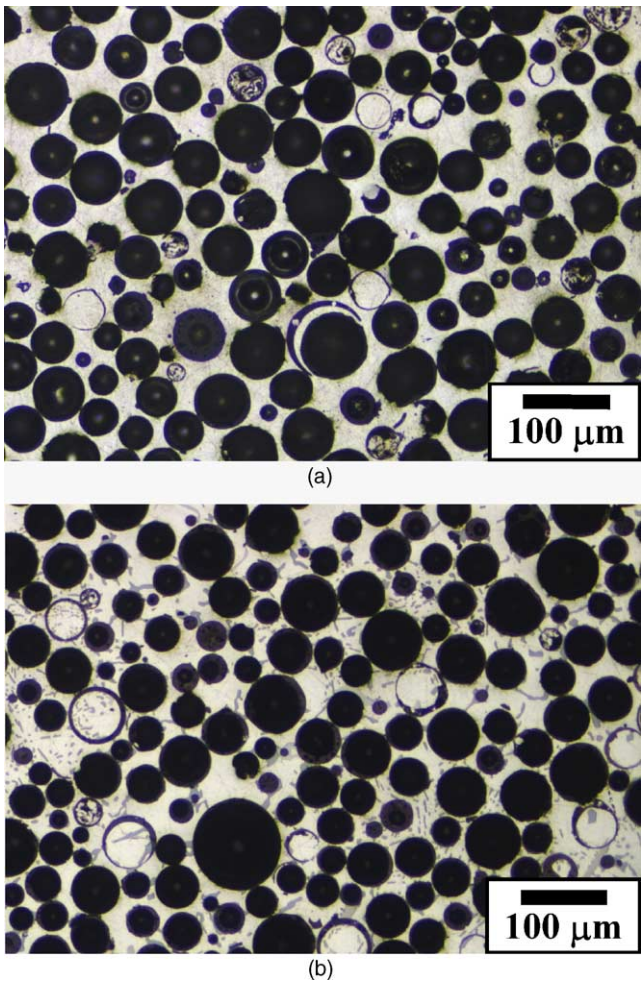

Fig. 1. (a) Microstructure of cp-Al syntactic foam; (b) microstructure of Alloy-T6 syntactic foam.

3. Results

3.1. Microstructures

Representative micrographs of typical syntactic foams are shown in Fig. 1a and b. Due to changes in matrix chemistry, discussed in Section 4.1, the 7075-Al foams are hereafter referred to simply as "Alloy-O" and "Alloy-T6" in both the text and figures. The Alloy-O foam has qualitatively the same microstructure as the Alloy-T6 material. The microspheres are uniformly distributed, with an average diameter of ca. 50 μm. Some infiltrated spheres are observed, 4.4% of the total number of spheres for the cp-Al foam and 9.3% for the alloy foams (determined by counting ca. 6000 spheres on polished sections). Some sphere fragments are also visible, and are believed to have been fractured either when received or during either packing or infiltration. Also seen in the alloy foams are dark gray inclusions, determined to be silicon by EDS analysis, and with a volume fraction of ca. 10%, as determined by image analysis. The average cp-Al and alloy foam densities were 1.40 and 1.66 ± 0.02 g/cm^3, respectively, corresponding to relative densities of 0.52 and 0.59 as compared to fully-dense cp-Al and 7075-Al matrices.

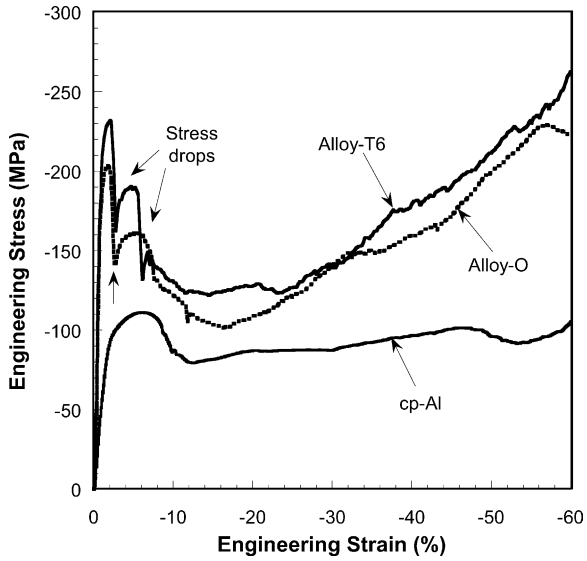

Fig. 2. Quasi-static compressive behavior of the cp-Al and alloyed syntactic foams. Stress drops corresponding to the formation of 45° crush-bands are indicated with arrows.

3.2. Mechanical properties

Representative quasi-static engineering stress–strain curves are shown in Fig. 2. Typical ductile foam behavior is observed [1,2], i.e., an initial approximately linear region culminating in a peak stress, a drop in stress corresponding to the onset of cell densification, an extended plateau at roughly constant stress where cells densify plastically, and an upward turn of the stress–strain curve at the completion of densification. The stress–strain behavior of 2–4 foam samples of each type was measured, with consistent results varying not more than 10% for the peak strengths. On average, the cp-Al foam reached a peak strength of −109 MPa before the onset of densification. The densification plateau stress was measured to be between −80 and −100 MPa until an engineering strain of −60% was reached; beyond this point, densification was essentially complete and stress increased continuously with increasing strain. The Alloy-O and Alloy-T6 foams reached considerably higher peak strengths (−199 and −229 MPa, respectively) prior to the transition into the densification plateau. Following two sharp stress drops at strains below −10%, densification proceeded at stresses between −100 and −140 MPa until engineering strains of −25 to −30% were reached.

Typical engineering stress–strain curves for the high-strain rate tests are shown in Fig. 3a–c to final strains between −11 and −14%. The quasi-static behavior up to strains of −15% are included for comparison. The cp-Al, Alloy-O, and Alloy-T6 foams reached peak strengths of −140, −231, and −248 MPa, respectively (average of two samples of each material), with the Alloy-T6 foam proceeding into a densifica-

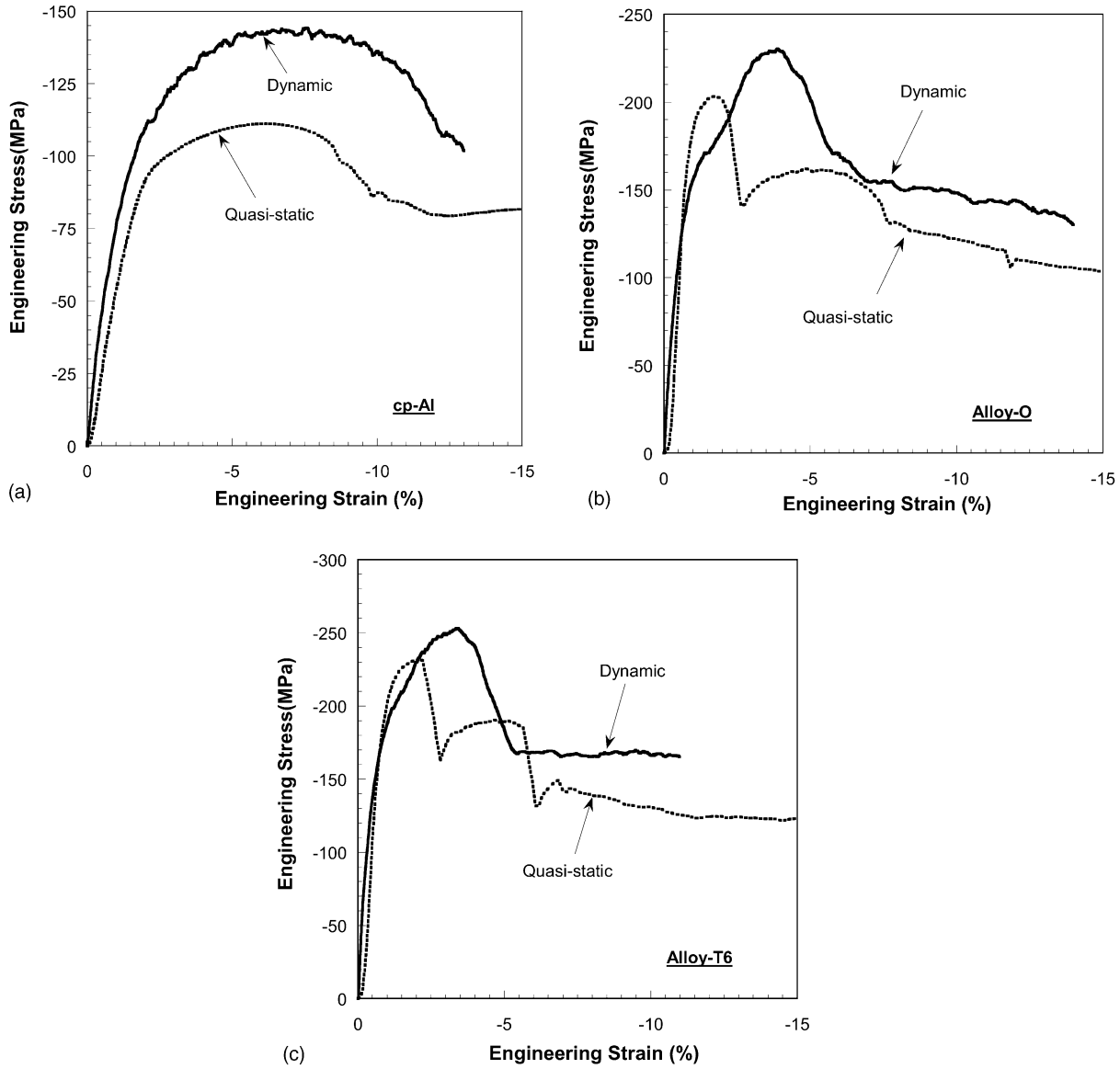

Fig. 3. (a) Dynamic compressive behavior of the cp-Al syntactic foam; (b) dynamic compressive behavior of the Alloy-O syntactic foam; (c) dynamic compressive behavior of the Alloy-T6 syntactic foam.

tion plateau at ca. −170 MPa. The cp-Al and Alloy-O foams did not enter a true plateau for the total plastic strains reached during dynamic testing.

3.3. Post-compression X-ray tomography

Images assembled from the X-ray tomography data sets are shown in Fig. 4a–d for the cp-Al and Alloy-T6 foams pre-strained quasi-statically to strains of −9 and −8%, respectively. Fig. 4a and b shows sections taken through the entire height of the compression samples. These images show the sample microstructures through the vertical center plane of each sample, with a vertical compression axis in both images. Fig. 4c and d are higher-magnification sections of Fig. 4a and b taken near the centers of those slices, showing the densified regions in the center of each sample. In all images, both hollow and infiltrated spheres can clearly be distinguished, as well as deformed (ellipsoidal) pores in the cp-Al foam. Two compression or “shear” bands with fully collapsed pores are visible in the Alloy-T6 foam, while the deformation is more diffuse in the cp-Al foam which shows extensive barreling and pore compression.

4. Discussion

4.1. Microstructure

As seen in Fig. 1, infiltration of the open space between microspheres was very nearly complete, with no visible

porosity remaining between spheres. There were some infiltrated spheres, ca. 5–10% of the total sphere population depending on the matrix. These spheres were either cracked prior to or during infiltration, or had thin regions of amorphous silica that dissolved in the molten aluminum [21]. Evidence for the dissolution of silica is seen in the formation of blocky gray silicon inclusions precipitated throughout the matrix in the Alloy-T6 foam (Fig. 1b); no such silicon inclusions are visible in the cp-Al foams. This difference in microstructure can be rationalized on the basis of differences in solidification characteristics, the large freezing range of the starting 7075-Al matrix ($T_{liquidus}$ = 635 °C, $T_{solidus}$ = 477 °C [18]) giving rise to considerably longer solidification times after infiltration, resulting in more time for sphere dissolution in the melt. Also present in the Alloy-T6 foams are light gray inclusions with a much smaller volume fraction (1–2%), identified by EDS as an Al–Cr–Fe intermetallic, and which were probably due to reaction with impurities in the spheres, or to normal impurities in the alloy (which contains 0.18–0.28% Cr and up to 0.50% Fe [22]). In both types of foams, merged or nested spheres are observed, but due to their infrequency their effect on the bulk mechanical properties is assumed in this study to be negligible.

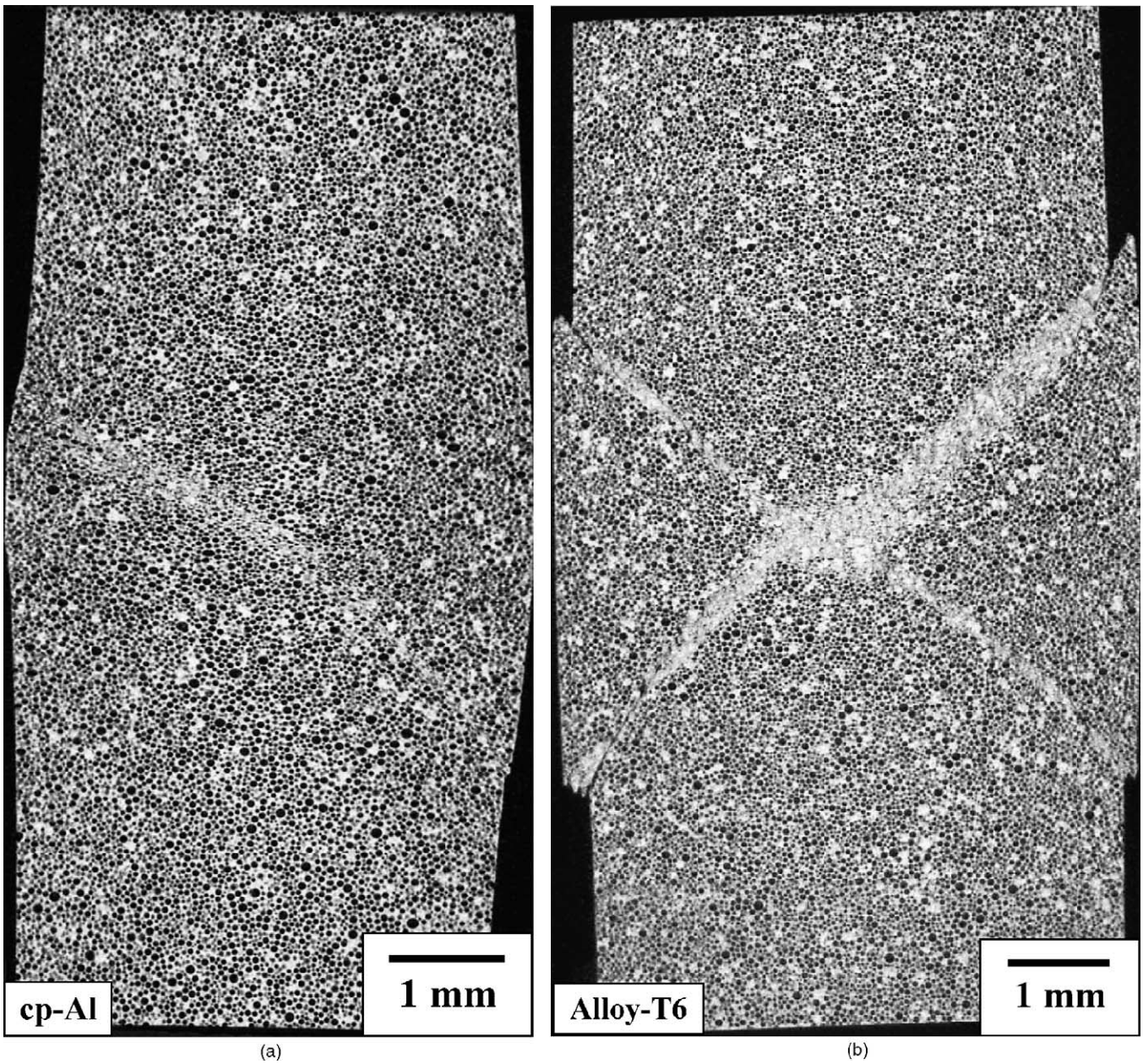

Fig. 4. (a) X-ray tomography slice of cp-Al foam, pre-strained quasi-statically to −9% strain; (b) X-ray tomography slice of Alloy-T6 foam, pre-strained quasi-statically to −8% strain; (c) and (d) magnified details of (a) and (b) showing central crush zones.

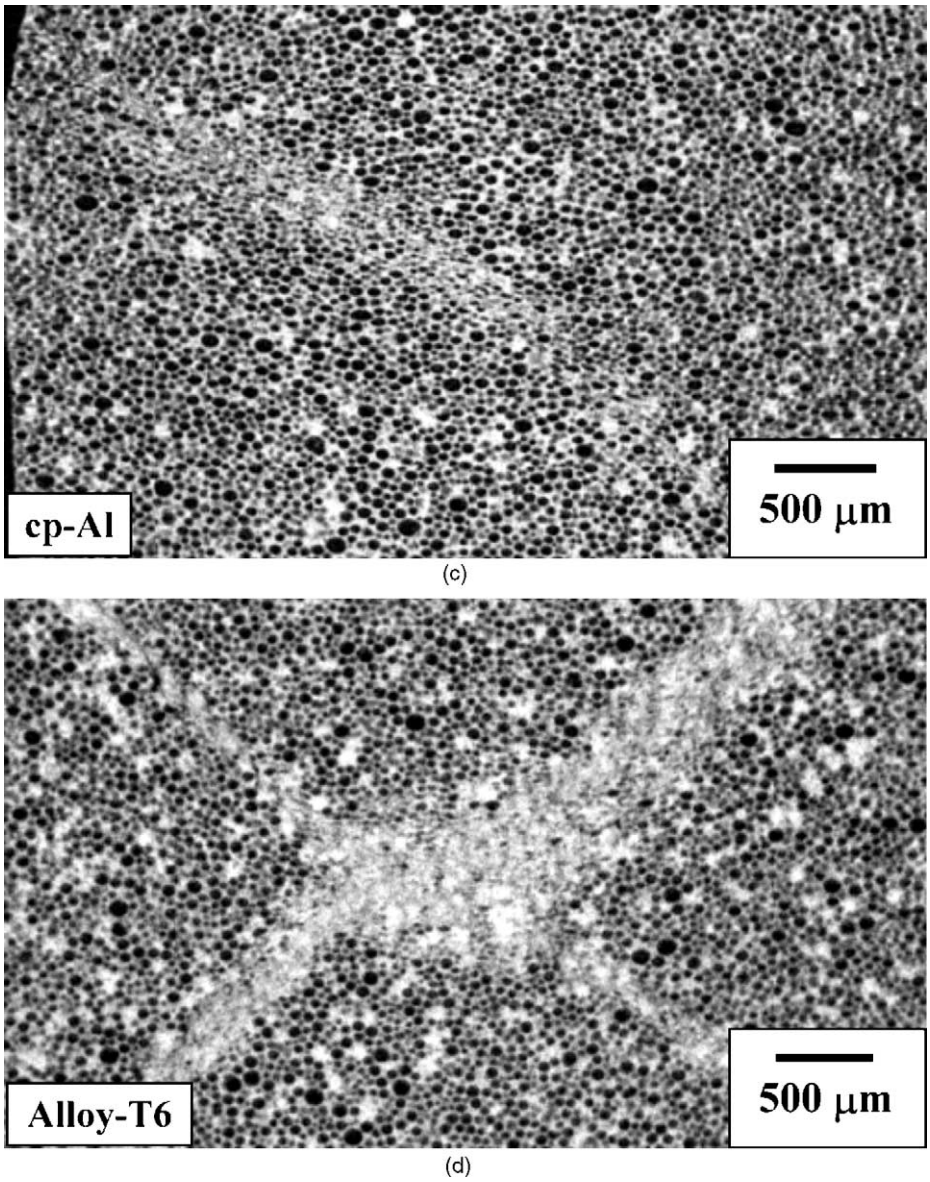

Fig. 4. (*Continued*).

What cannot be neglected, however, are the changes to the original chemistry and microstructure of the aluminum matrices due to reaction between the melt and the spheres after infiltration. In the case of the cp-Al foam, the originally unalloyed matrix apparently acquired only a minimal amount of silicon, removed from the spheres during the relatively brief time (ca. 5 min) between infiltration and solidification. More significantly, the initially 7075-Al matrix incorporated a much larger amount of silicon during its longer solidification time (ca. 20 min). Based on the measured volume fractions of aluminum and silicon (0.30 and 0.10, respectively) in the alloy foams, the mass fraction of silicon in the resultant matrix was approximately 23%. The adjusted composition of the aluminum matrix is therefore approximately (in wt.%) 23% Si, 4% Zn, 2% Mg, 1% Cu, 0.15% Cr, and ca. 70% Al. This composition is far from that of 7075-Al (5.6% Zn, 2.5% Mg, 1.6% Cu, 0.23% Cr, <0.40% Si), and is closest to the 390 series of aluminum casting alloys (typically 17% Si, 0.1% Zn, 0.55% Mg, 4.5% Cu, and 1.0% Fe) [22]. We therefore refer to the nominally 7075-Al foams simply as "Alloyed". Typical yield strengths for A390 permanent mold castings are 200 and 310 MPa in the F (as-fabricated) and T6 tempers [22]. These values are considerably closer together than the yield strengths for 7075-Al in the O (103 MPa) and T6 (503 MPa) tempers, and might explain the relatively modest effect of heat treatment on the mechanical properties of the alloy foams, as seen in Fig. 2. Also potentially contributing to the relatively small difference between Alloy-O and Alloy-T6 is that the standard T6 temper for the 390 series of casting alloys is 8 h at 175 °C, compared to the 36 h at 120 °C used in this study; the Alloy-T6 material is therefore most likely not in a "peak-aged" condition. If the alloyed foams were

to be cooled after infiltration more rapidly than the present rate of 10 °C/min, it is likely that reductions in sphere dissolution and silicon precipitation would be observed, with a concomitant improvement in mechanical properties.

4.2. Quasi-static compression and energy absorption

During quasi-static compression, Fig. 2, the cp-Al and alloyed foams exhibited different modes of failure at the peak stress and during densification. The cp-Al foam showed barreling at the center of the sample prior to reaching the peak stress, leading to the rounded shape of the peak in the stress–strain curve. This was in contrast to the sharp primary drop and slightly more rounded secondary drop in the stress–strain curves of the alloyed materials, which were the result of two near-45° "shear" bands of collapsed spheres forming in the specimens, most likely due to the higher strength and reduced ductility of the alloyed matrices containing strong, brittle silicon reinforcement. The lower strain at which densification appeared complete and the region of slowly increasing stress during compression between engineering strains of −25 to −60% in the alloyed foams may be attributed to the reduced matrix ductility. After a brief initial period of microsphere collapse and limited matrix plastic flow, higher stresses were required to deform the alloyed matrix into the voids created by microsphere cracking.

Energy absorption during densification was exceptionally high for all the tested foams. The energy absorbed during compression to the densification strain was 55 J/cm^3 (at $\varepsilon = -60\%$) and 36 J/cm^3 (at $\varepsilon = -25\%$) for the cp-Al and Alloy-T6 foams, respectively. Extending the considered region of the stress–strain curve to the point at which the plateau stress exceeds the peak stress, the value for energy absorption in the Alloy-T6 foam increases to 80 J/cm^3 at a strain of −55%. These values are an order of magnitude higher than those observed for low-density aluminum foams with relative densities $\rho_{rel} = 0.10$ and 0.25 [23–25], are significantly higher (by a factor of 2–3) than those observed for unreinforced aluminum foams of similar density [26], and are comparable to energy absorption values for steel foams produced by powder metallurgy [27]. These steel foams have similar relative densities ($\rho_{rel} = 0.38$–0.64), but far greater absolute densities (3.2–5.0 g/cm^3), than the aluminum foams discussed here. Even on a specific absorption basis, the energy absorption of these syntactic foams, 39 J/g for the cp-Al and 22 or 49 J/g (depending on strain) for the Alloy-T6 foam, compare favorably to both low-density aluminum foams as well as the polymeric foams currently used in packaging applications [1]. Their much higher strengths, however, makes them useful in applications where permanent deformation at low stresses is undesirable, e.g., for automotive bumpers.

4.3. Dynamic compression and strain rate sensitivity

To assure valid high-rate measurements on this material, it is necessary to examine the different analyses used to calculate specimen stress from the Hopkinson bar strain. In the one-wave analysis the specimen stress is directly proportional to the bar strain measured from the transmitted bar. The one-wave stress analysis reflects the conditions at the sample-transmitted bar interface and is often referred to as the specimen "back stress". This analysis results in stress–strain curves with small oscillations, especially near the yield point. Alternatively in a two-wave analysis, the sum of the synchronized incident and reflected bar waveforms (which are opposite in sign) is proportional to the specimen "front stress" and reflects the conditions at the incident/reflected bar-sample interface. The equations for converting these signals into stress and strain are described elsewhere [28]. Finally, a third stress-calculation variation that considers the complete set of three measured bar waveforms, the three-wave analysis, is simply the average of the two-wave "front" and the one-wave "back" stress. A valid uniaxial stress Hopkinson bar test requires that the stress state throughout the specimen achieve equilibrium during the test and this condition can be checked readily by comparing the one-wave and two-wave stress–strain response. When the stress state is uniform throughout the specimen, then the two-wave stress oscillates about the one-wave stress [28]. Additionally, a relatively constant strain rate is also desirable: gradually increasing or decreasing strain rates indicate that either too much or too little energy, respectively, is available for deformation. For the current study only tests meeting these criteria were deemed acceptable. The use of shorter specimens (length/diameter ratio of 1.0) in the dynamic compression testing as compared to the quasi-static testing (length/width ratio of 2.2) is not expected to impact the measured peak strengths, based on previous work on pure aluminum which showed frictional effects to only become problematic at L/D ratios of 0.5 and below [29].

The compressive behavior of both types of foam at high strain rates, Fig. 3, were found to be very reproducible (peak stress to within 10 MPa), and exhibited peak strengths that are 10–30% higher than those measured during quasi-static testing, as well as a higher plateau stress (ca. −170 versus −120 to −140 MPa) for the Alloy-T6 foam. Adiabatic heating during the dynamic testing has been neglected; the majority of the work done during dynamic plastic deformation is converted to heat [30], but at the relatively low strains reached at the foam peak strengths it is assumed that sample heating is minimal. Interestingly, compression at high strain rates appears to suppress the stress drops associated with the formation of the sharp "shear" bands of compressed spheres oriented 45° to the compression axis in the alloyed foams; as seen in Fig. 3b and c, the transition into the constant-stress densification plateau becomes smoother and closer in nature to that of the cp-Al material. Dynamic loading also appears to shift the location of the peak stress to slightly higher strains for all three foams, which can be rationalized as a result of the strain rate sensitivity of the foam matrices allowing slightly higher yield strengths, and therefore strains, to be reached prior to the onset of collapse. The increases in peak and plateau stress at high strain rates lie mid-range in comparison with the widely

varying strain rate effects reported for aluminum foams; increases in peak strength between 50 and 150% during dynamic testing of Alporas foams [31,32] and Al foams formed by powder metallurgy [33] have been reported, as has the lack of strain rate effects in Duocel [32], Alulight [34], and Fraunhofer [35] aluminium foams. aluminum foams.

The strain rate sensitivity of materials can be quantified using a sensitivity parameter Σ, defined as [36]:

$$\Sigma = \frac{\sigma_d - \sigma_q}{\sigma^*} \frac{1}{\ln(\dot{\varepsilon}_d/\dot{\varepsilon}_q)} \quad (1)$$

where σ is the stress at a given strain, σ^* the stress at a given strain at a reference strain rate of $10^{-3}\,s^{-1}$, $\dot{\varepsilon}$ the strain rate, and the subscripts d and q refer to dynamic and quasi-static testing, respectively. Generally the flow stress at 5% strain is used for σ^*; foam materials, however, can exhibit abrupt variations in stress during compression that are not seen in alloys or composites with monotonic behavior at low to moderate strains. The peak stress reached during compression was therefore used in the calculations of Σ, even though these peak stresses occurred at slightly different strains. The average peak stresses reached during both dynamic and quasi-static testing and the resulting Σ parameters are summarized in Table 1. In agreement with results for a wide variety of aluminum alloys, as reviewed in Ref. [36], Σ decreases as a function of increasing matrix strength, and the values for Σ calculated here are in line with those measured for, e.g., 1100 wrought aluminum (99% Al, 1% Si + Fe) in the case of the cp-Al foams, and 359 casting aluminum (9% Si, 0.6% Mg) with yield stresses of 200–250 MPa in the case of the alloyed foams. This indicates that the high volume fraction of mullite spheres does not affect significantly the strain rate sensitivity of the foam, which is controlled by the strength of the matrix, as was also observed by San Marchi et al. [36] when comparing aluminum alloys with aluminum matrix composites.

4.4. X-ray tomography of quasi-statically deformed microstructures

The use of X-ray tomography provides two significant advantages: (a) the entire deformed sample can be examined, rather than individual slices examined metallographically, and (b) there is no risk of introducing preparation artifacts, which is especially important in porous materials with pre-existing damage. The X-ray tomography slices through the cp-Al and Alloy-T6 compression samples, Fig. 4, clearly show the differences in the deformation behavior of these materials. These differences can be linked to features on the stress–strain curves for these foams, Fig. 2. The sharp stress drops after the peak stress in the Alloy-T6 foam correspond to the formation of the two localized deformation bands of heavily crushed material oriented at ca. 45° with respect to the compression axis, along the direction of the maximum shear stress. Similar behavior has been noted during compression of polymeric syntactic foams [6], as well as in aluminum metal matrix composites [36,37]. The cp-Al foam, conversely, exhibits a much more graceful transition into the densification plateau, exhibiting extensive barreling and pore deformation over a much larger volume.

Table 1
Foam peak stresses and sigma parameters

Foam matrix	Quasi-static peak stress (MPa)	Dynamic peak stress (MPa)	Foam sigma parameter (–)	Matrix sigma parameter (–)
cp-Al	−109	−140	0.019	0.015–0.018[a]
Alloy-O	−199	−231	0.011	0.009[b]
Alloy-T6	−229	−248	0.006	0.009[b]

[a] For Al-1100 [36].
[b] For Al-359 [36].

Damage is thus distributed very differently in the two foams. In the cp-Al foam, damage is spread over the very large bulged region (visible as ca. 40% of the specimen volume in Fig. 4a) and is characterized by a rather uniform but modest plastic deformation of the matrix coupled with sphere fracture, which can be deduced from the oblate shape of the pores in Fig. 4c. A thin crush-band where strain is much higher is also visible in that figure, but it represents only a small contribution to the total strain in the bulged region. In contrast, in the Alloy-T6 foam, damage is concentrated in the two much thicker crush-"shear" bands. In these bands, strain is very high, as illustrated by the complete collapse of the pores. Plastic strain outside the crush-bands is minimal, as deduced by the spherical shape of the pores (Fig. 4b and d), whose mullite microspheres may still be intact.

This difference in failure mode can be explained qualitatively based on the different strengths of the matrices. For the cp-Al foam, matrix plasticity occurs at low applied stresses before microsphere stresses are high enough to induce fracture. Rather, matrix plasticity results in a large plastic mismatch with, and increased load transfer to, the microspheres and their eventual fracture. Foam deformation then takes place over a large volume, in a manner similar to that in some traditional foams without microspheres, or in metal matrix composites with non-hollow reinforcement. For the alloyed foams, the higher-strength matrix remains elastic to higher applied stress, and elastic load transfer (expected to be similar to load transfer in metal matrix composites) leads to fracture of the microspheres before the onset of "bulk" matrix plasticity. The fracture stress of the spheres is also probably reduced by the chemical reaction with the matrix, as described earlier. Rapid propagation of sphere fracture takes place over a first crush-band, with a concomitant transfer of stress to the matrix adjacent to the crushed spheres. This matrix is unable to sustain the increased stress and thus plastically deforms until it fills the pores unsupported by the crushed microspheres. The second perpendicular crush-"shear" band forms at lower stresses, as it can nucleate from the first crush-band.

In summary, foam plastic deformation is controlled by the weaker of the two phases, the metallic matrix (for the cp-Al

foams) or the ceramic microspheres (for the alloyed foams). Subsequent damage evolution (localized crush-bands or diffuse bulging) is controlled by the very different plastic behavior of these phases: extensive plasticity in the matrix and brittle fracture of the microspheres. A mechanically-optimized syntactic foam is then one where microsphere collapse occurs at the same stress as matrix plastic yield. This is dictated by the intrinsic mechanical properties of the phases, the sphere geometry (diameter, wall thickness), and the load transfer between the phases, which is itself controlled by the volume fractions of each phase and the spatial distribution/connectivity of spheres, as well as the nature of the metal–ceramic interfacial bonding.

5. Conclusions

Aluminum matrix / hollow ceramic microsphere syntactic foams were fabricated by liquid metal infiltration of commercially pure and 7075 aluminum. The cp-Al foam exhibited peak strengths in compression of over −100 MPa, with a uniform densification plateau to −60% strain. Although the composition of the 7075-Al matrix was altered by dissolution of silicon from the microsphere reinforcement, both the annealed and heat-treated alloyed matrix foams had significantly higher peak strengths, up to −230 MPa, relative to the cp-Al foam.

Dynamic compression testing showed a 10–30% increase in peak strength compared to the quasi-static results; the strain rate sensitivities of these foams are similar to those of aluminum matrix composite materials. These foams displayed excellent energy-absorbing capability, which suggests their potential use in packaging applications or for impact protection in situations where a high plateau stress is desired. X-ray tomographic investigation of the post-compression foam microstructures revealed sharp differences in deformation mode, with the cp-Al foam deforming in a gradual manner by large-scale matrix plasticity, whereas the alloyed foams exhibited two abrupt stress drops from the formation of sharp crush-"shear" bands triggered by sphere fracture.

Optimized syntactic foam properties are predicted when the matrix and microsphere strengths are properly matched through judicious choice of matrix strength (through composition and heat treatment), microsphere strength (through their material, diameter, and wall thickness) and load transfer between the two phases (through phase volume fraction, interfacial strength, and phase spatial distribution and connectivity).

Acknowledgments

DKB acknowledges the Department of Defense for support in the form of an NDSEG Fellowship. JOD acknowledges the International Collaboration Programme from Enterprise Ireland. GRD acknowledges support from The Engineering and Physical Sciences Research Council, UK (EPSRC grant No. GR/R28911). GTG III and CMC acknowledge a portion of this study was conducted under the auspices of the U.S. Department of Energy. The authors thank Mr. Paul Seshold (Enviraspheres Pty Ltd.) for providing microspheres.

References

[1] L.J. Gibson, M.F. Ashby, Cellular Solids, Structure and Properties, second ed., Cambridge University Press, Cambridge, UK, 1997.
[2] M.F. Ashby, A. Evans, N.A. Fleck, L.J. Gibson, J.W. Hutchinson, H.N.G. Wadley, Metal Foams: A Design Guide, Butterworths/Heinemann, Boston, MA, 2000.
[3] J. Banhart, Prog. Mater. Sci. 46 (2001) 559–632.
[4] F.A. Shutov, Adv. Polym. Sci. 73–74 (1986) 63–123.
[5] P. Bunn, J.T. Mottram, Composites 24 (1993) 565–571.
[6] N. Gupta, E. Kishore, S. Woldesenbet, Sankaran, J. Mater. Sci. 36 (2001) 4485–4491.
[7] P.K. Rohatgi, R.Q. Guo, H. Iksan, E.J. Borchelt, R. Asthana, Mater. Sci. Eng. A 244 (1998) 22–30.
[8] M. Kiser, M.Y. He, F.W. Zok, Acta Mater. 47 (1999) 2685–2694.
[9] T. Miyoshi, M. Itoh, S. Akiyama, A. Kitahara, Adv. Eng. Mater. 2 (2000) 179–183.
[10] C. San Marchi, A. Mortensen, Acta Mater. 49 (2001) 3959–3969.
[11] M. Hartmann, K. Reindel, R.F. Singer, Mater. Res. Soc. Symp. Proc. 521 (1998) 211–216.
[12] D.K. Balch, D.C. Dunand, in: A. Ghosh, T. Sanders, D. Claar (Eds.), Processing and Properties of Lightweight Cellular Metals and Structures, TMS, Warrendale, PA, 2002, pp. 251–260.
[13] H. Bart-Smith, A.-F. Bastawros, D.R. Mumm, A.G. Evans, D.J. Sypeck, H.N.G. Wadley, Acta Mater. 46 (1998) 3583–3592.
[14] A.-F. Bastawros, H. Bart-Smith, A.G. Evans, J. Mech. Phys. Solids 48 (2000) 301–322.
[15] O.B. Olurin, M. Arnold, C. Korner, R.F. Singer, Mater. Sci. Eng. A 328 (2002) 334–343.
[16] L. Salvo, P. Cloetens, E. Maire, S. Zabler, J.J. Blandin, J.Y. Buffière, W. Ludwig, E. Boller, D. Bellet, C. Josserond, Nucl. Instrum. Meth. Phys. Res., Sect. B: Beam Interact. Mater. Atoms 200 (2003) 273–286.
[17] A. Mortensen, I. Jin, Int. Mater. Rev. 37 (1992) 101–128.
[18] J.E. Hatch (Ed.), Aluminum: Properties and Physical Metallurgy, ASM International, Metals Park, OH, 1984.
[19] G.T. Gray III, D.J. Idar, W.R. Blumenthal, C.M. Cady, P.D. Peterson, Proceedings of the 11th International Symposium on Detonation, Snowmass Village, CO, 31 August–4 September 1998.
[20] G.R. Davis, J.C. Elliott, J. Phys. IV 104 (2003) 131–134.
[21] R.Q. Guo, P.K. Rohatgi, Metall. Mater. Trans. 29B (1998) 519–525.
[22] Metals Handbook, vol. 2, tenth ed., ASM International, Materials Park, OH, 1990.
[23] F. Han, Z. Zhu, J. Gao, Metall. Mater. Trans. 29A (1998) 2497–2502.
[24] T. Miyoshi, M. Itoh, T. Mukai, H. Kanahashi, H. Kohzu, S. Tanabe, K. Higahi, Scripta Mater. 41 (1999) 1055–1060.
[25] A.E. Markaki, T.W. Clyne, Acta Mater. 49 (2001) 1677–1686.
[26] Y.Y. Zhao, D.X. Sun, Scripta Mater. 44 (2001) 105–110.
[27] C. Park, S.R. Nutt, Mater. Sci. Eng. A 288 (2000) 111–118.
[28] G.T. Gray III, in: H. Kuhn, D. Medlin (Eds.), ASM Metals Handbook, vol. 8: Mechanical Testing and Evaluation, ASM International, Metals Park, OH, 2000, pp. 462–476.
[29] J.Z. Malinowski, J.R. Klepaczko, Int. J. Mech. Sci. 28 (1986) 381–391.
[30] R. Kapoor, S. Nemat-Nasser, Mech. Mater. 27 (1998) 1–12.

[31] T. Mukai, H. Kanahashi, T. Miyoshi, M. Mabuchi, T.G. Nieh, K. Higashi, Scripta Mater. 40 (1999) 921–927.
[32] K.A. Dannemann, J. Lankford, Mater. Sci. Eng. A 293 (2000) 157–164.
[33] F. Yi, Z. Zhu, F. Zu, S. Hu, P. Yi, Mater. Charact. 47 (2001) 417–422.
[34] V.S. Deshpande, N.A. Fleck, Int. J. Impact Eng. 24 (2000) 277–298.
[35] I.W. Hall, M. Guden, C.-J. Yu, Scripta Mater. 43 (2000) 515–521.
[36] C. San Marchi, F. Cao, M. Kouzeli, A. Mortensen, Mater. Sci. Eng. A 337 (2002) 202–211.
[37] M. Guden, I.W. Hall, Scripta Mater. 39 (1998) 261–267.